Dalton Transactions

PAPER

View Article Online
View Journal | View Issue

Check for updates

Cite this: *Dalton Trans.*, 2017, **46**, 9201

Interconnected hierarchical $NiCo_2O_4$ microspheres as high-performance electrode materials for supercapacitors†

Ming Cheng,[a] Hongsheng Fan,[a] Yuanjun Song,[b] Yimin Cui [a] and Rongming Wang *[b]

Herein, interconnected hierarchical $NiCo_2O_4$ microspheres (IH-$NiCo_2O_4$) were prepared *via* a solvothermal method followed by an annealing treatment. IH-$NiCo_2O_4$ possesses large tunnels and abundant mesopores, which are in favor of their applications in energy storage field. When employed as an electrode material for supercapacitors, IH-$NiCo_2O_4$ exhibits a high specific capacitance of 1822.3 F g^{-1} at a current density of 2 A g^{-1}, an excellent rate property of 68.6% capacity retention at 20 A g^{-1}, and an 87.6% specific capacitance retention of its initial value after 7000 cycles at a high current density of 10 A g^{-1}, superior to those of IH-Co_3O_4. Furthermore, an optimal asymmetric supercapacitor (ASC) was also constructed with IH-$NiCo_2O_4$ as the positive electrode and graphene as the negative electrode. The ASC delivers a high energy density of 39.4 Wh kg^{-1} at a power density of 800 W kg^{-1}. Even at a high power density of 8000 W kg^{-1}, the energy density still reaches 27.2 Wh kg^{-1}. Moreover, the ASC shows a good cycling stability with 80.1% specific capacitance retention after 5000 cycles at 6 A g^{-1}. The excellent electrochemical performance of IH-$NiCo_2O_4$ makes it a promising electrode material in energy storage field.

Received 11th April 2017,
Accepted 21st June 2017

DOI: 10.1039/c7dt01289f

rsc.li/dalton

Open Access Article. Published on 21 June 2017. Downloaded on 9/23/2024 5:19:20 PM.
This article is licensed under a Creative Commons Attribution 3.0 Unported Licence.

Introduction

Owing to the inevitable exhaustion of fossil fuels, ever-deteriorating environment, and fast-growing energy demand, the development of renewable, environmentally friendly, and efficient energy storage technologies has attracted significant attention.[1–3] Among various energy storage systems, supercapacitors have occupied an indispensable position due to their high power density, improved safety, and long-life stability.[4,5] Supercapacitors are commonly divided into two categories: electrical double-layer capacitors (EDLCs) and pseudocapacitors.[6] Considering the energy storage mechanisms, pseudocapacitors that are mainly based on reversible Faradaic redox reactions deliver higher energy density than the typical EDLCs, which only relies on charge accumulation at the surface of electrode materials.[7,8] However, currently, pseudocapacitors still suffer from low energy density and poor long-life cycling that limit their practical applications. Considering this, numerous efforts have been devoted towards exploring attractive electrode materials that can provide higher energy density and longer life span without sacrificing high power density.[2,9–14]

Among the pseudocapacitive materials, spinel $NiCo_2O_4$ has drawn significant interest due to its many advantages such as rich redox reactions involving different cations, environmental friendliness, low-cost, and abundant resources.[15–18] Moreover, owing to the co-existence of two different metal cations in a single crystal structure, $NiCo_2O_4$ can synergistically enhance the electrochemical performance as compared to the corresponding nickel oxides and cobalt oxides.[15,19–22] For example, An *et al.* demonstrated that the porous $NiCo_2O_4$ nanowires exhibited higher capacitance than Co_3O_4 with a similar structure.[19] More recently, Hu *et al.* also reported that Co_3O_4/$NiCo_2O_4$ double-shelled nanocages showed improved pseudocapacitance than the single-component Co_3O_4/Co_3O_4 double-shelled nanocages.[23] These excellent features disclose the development potential of $NiCo_2O_4$ as a promising electrode material for supercapacitors.

As is well-known, the electrochemical performance of electrode materials also strongly depends on their microstructures, which influence the porosity and specific surface area.[9,24–27] $NiCo_2O_4$ materials with diverse structures,[28,29] such as porous nanowires,[19] mesoporous nanosheets,[4] hierarchical hollow nanocubes,[18] hierarchical tetragonal microtubes,[30] hollow spheres,[31] and urchin-like microspheres,[32] have been synthesized, and they exhibit a distinct difference in their capacitance performance. Therefore, it is a practical strategy to

[a]*Department of Physics, Beihang University, Beijing 100191, P. R. China*
[b]*Beijing Key Laboratory for Magneto-Photoelectrical Composite and Interface Science, School of Mathematics and Physics, University of Science and Technology Beijing, Beijing 100083, P. R. China. E-mail: rmwang@ustb.edu.cn*

†Electronic supplementary information (ESI) available. See DOI: 10.1039/c7dt01289f

Open Access Article. Published on 21 June 2017. Downloaded on 9/23/2024 5:19:20 PM.
This article is licensed under a Creative Commons Attribution 3.0 Unported Licence.

explore an appropriate structural $NiCo_2O_4$ to achieve high supercapacitance performance. Considering the similar structural requirements of electrode materials for Li-ion-based batteries and supercapacitors, the structure with excellent performance for one can be applied in the other one. For example, yolk-shelled Ni–Co mixed oxide nanoprisms,[15] $NiCo_2O_4$ complex hollow spheres,[31] Mn-based mixed metal oxide hierarchical tubular structures,[20] and UNF@$NiCo_2O_4$ composites[22] have been demonstrated to possess excellent performance in both fields. Thus, a material with large tunnels and mesopores, which has been proved to exhibit high performance for Li–O_2 batteries,[33] is a promising alternative electrode material for supercapacitors.

Herein, we synthesized an IH-$NiCo_2O_4$ with large tunnels and mesopores *via* a facile solvothermal process followed by an annealing treatment in an air atmosphere at 200 °C. IH-$NiCo_2O_4$ exhibits a high specific capacitance of 1822.3 F g^{-1} at 1 A g^{-1}, much higher than that of IH-Co_3O_4. After 7000 continuous cycles at 10 A g^{-1}, IH-$NiCo_2O_4$ retains an 87.6% specific capacitance retention of its initial value. Furthermore, an optimized asymmetric supercapacitor IH-$NiCo_2O_4$//graphene was fabricated and showed high capacitance, excellent rate property, and good cycling stability. These results indicate that IH-$NiCo_2O_4$ is a promising pseudocapacitance material for supercapacitors.

Experimental

Chemicals

Cobaltous nitrate hexahydrate ($Co(NO_3)_2{\cdot}6H_2O$, ≥96%), nickel(II) nitrate hexahydrate ($Ni(NO_3)_2{\cdot}6H_2O$, ≥98%), isopropanol (IPA, C_3H_8O, ≥99.6%), ethylene glycol (EG, $C_2H_6O_2$, ≥99%), and ethanol (C_2H_6O, ≥99.6%) were purchased from Beijing Chemical Reagents Company. Deionized water was purchased from Beijing Deionized Water Company. All chemicals were of analytical grade and used as received without further purification. Graphene was purchased from Nanjing XFNANO. Materials Tech Co., Ltd.

Preparation of materials

In a typical synthesis of nickel–cobalt glycolate, first, 0.194 g $Co(NO_3)_2{\cdot}6H_2O$ and 0.097 g $Ni(NO_3)_2{\cdot}6H_2O$ were placed in a 100 mL Teflon container. Second, 25 mL IPA, 35 mL EG, and 1 mL deionized water were added one after another to a container under stirring for 10 min after each addition. The container was then transferred to a stainless steel autoclave and kept in an electrical oven at 190 °C for 12 h. After being naturally cooled down to room temperature, the precipitate was separated *via* centrifugation, washed several times, and dried in an oven at 80 °C overnight. Then, the precursor was calcined at 200 °C in air for 2 h at a heating rate of 1 °C min^{-1} to obtain IH-$NiCo_2O_4$. To prepare IH-Co_3O_4, 0.291 g $Co(NO_3)_2{\cdot}6H_2O$ was added to a Teflon container and mixed with 30 mL IPA, 30 mL EG, and 1 mL deionized. The subsequent process was similar to that of IH-$NiCo_2O_4$.

Characterization of materials

The crystal structure, morphologies, chemical compositions, and chemical state of the as-synthesized products were studied *via* X-ray diffraction (XRD, X'Pert Pro MPD system, Cu Kα, λ = 0.154 nm), X-ray photoemission spectroscopy (XPS, ESCALAB MK II, Al Kα photon source, C 1s 284.8 eV), field-emission scanning electron microscopy (FESEM, HITACHI, S4800 and Carl Zeiss Supra 55 Ultra SEM), and transmission electron microscopy (TEM, JEOL 2200F with a field emission gun and an accelerating voltage of 200 kV). The specimen for the TEM study was prepared by dispersing a drop of alcohol solution containing the as-synthesized product onto a porous carbon film supported on a copper grid, and it was dried in a vacuum drying oven. Thermogravimetric and differential scanning calorimetry analyses were performed using a thermal analysis instrument (NETZSCH STA 449F3). The specific surface areas of the products were determined *via* N_2 adsorption–desorption isotherm measurements at 77 K (Micrometrics, ASAP 2020).

Electrochemical measurements

For the preparation of the working electrodes, the as-synthesized active materials were mixed with carbon black and polyvinylidene fluoride (PVDF) at a mass ratio of 7 : 2 : 1 in *N*-methyl-2-pyrrolidinone. The mixture was coated onto a clean nickel foam current collector (area ~1 cm^2) and dried in a vacuum oven at 80 °C for 12 h. The dried electrode was then pressed using a hydraulic press at a pressure of 10 MPa to serve as the working electrode. The electrochemical tests were carried out in both three-electrode and two-electrode configurations with 6 M KOH aqueous solution as an electrolyte. In the three-electrode electrochemical cell, the loading masses of IH-$NiCo_2O_4$ and IH-Co_3O_4 are about 2.1 mg cm^{-2} and 2.31 mg cm^{-2}, respectively. A Pt wire and a saturated calomel electrode were used as the counter and reference electrodes, respectively. In the two-electrode electrochemical system, an asymmetric supercapacitor was constructed by taking IH-$NiCo_2O_4$ as the positive electrode and graphene as the negative electrode. Electrochemical measurements were performed using an electrochemical workstation (CHI660D) *via* cyclic voltammetry (CV) and chronopotentiometry (CP). Electrochemical impedance spectroscopy (EIS) measurements were also carried out using this apparatus over a frequency range of 100 kHz–0.01 Hz at open circuit voltage with an AC amplitude of 5 mV.

Moreover, specific capacitance (C), energy density (E), and power density (P) were calculated from the discharge curves based on the following equations:[16,17,19,34]

$$C = I\Delta t/\Delta V \quad (1)$$

$$E = C\Delta V^2/2 \quad (2)$$

$$P = E/\Delta t \quad (3)$$

where I is the current density, Δt is the discharge time, and ΔV is the applied potential window. The capacitance, energy density, and power density of the constructed asymmetric

 This journal is © The Royal Society of Chemistry 2017

Open Access Article. Published on 21 June 2017. Downloaded on 9/23/2024 5:19:20 PM.
This article is licensed under a Creative Commons Attribution 3.0 Unported Licence.

supercapacitor were calculated based on the sum of the masses of the positive and negative electrode materials.

Results and discussion

The IH-$NiCo_2O_4$ microspheres were prepared by a facile solvothermal process followed by an annealing treatment in an air atmosphere. First, nickel–cobalt glycolate was synthesized as the precursor for the $NiCo_2O_4$ microspheres. Fig. 1(a–c) shows the scanning electron microscopy (SEM) images of nickel–cobalt glycolate. It can be observed that nickel–cobalt glycolate possesses an interconnected hierarchical spherical structure with a diameter of about 1 μm. Large tunnels can also be observed. The structure of the prepared precursor is sensitive to the solvent composition. Fig. S1† shows the SEM images of the precursors prepared using different solvent compositions. It can be seen that only the precursors synthesized with 25 mL IPA and 35 mL EG have a uniform interconnected hierarchical structure. The amount of water also significantly affects the morphology of the precursors (Fig. S2†). If no water is added to the system, only solid precursors would be obtained. If less amount of water is added, the size of the tunnels of the product would be too small. However, if more amount of water is added, only flower-like products would be formed. Thermogravimetric analysis (TGA) of the nickel–cobalt glycolate precursor is shown in Fig. S3.† A rapid weight loss is observed between ~180 and ~240 °C with a strong exothermic peak at ~235 °C, due to the decomposition of the precursor to $NiCo_2O_4$. After calcination in air at 200 °C for 2 h, the nickel–cobalt glycolate microspheres can be successfully converted into IH-$NiCo_2O_4$ with the same structure, as shown in Fig. 1(d–f). If the calcination temperature is too high, the interconnected hierarchical structure would severely shrink (Fig. S4†). The crystallographic structure of the as-prepared IH-$NiCo_2O_4$ was confirmed by XRD (Fig. S5a†). Obviously, the peaks at 31.1°, 36.7°, 44.6°, 59.1°, 64.4°, and 77° were detected, corresponding to the (220), (311), (400), (511), (440), and (533) lattice planes of the typical spinel phase $NiCo_2O_4$ (JCPDF no. 73-1702). The atomic ratio of Ni to Co was measured to be 0.51 *via* EDS (Fig. S5b†), which is close to the stoichiometric ratio of $NiCo_2O_4$.

Moreover, the IH-Co_3O_4 microspheres were also fabricated *via* the similar process. Fig. 2(a–c) shows the SEM images of cobalt glycolate. The interconnected hierarchical structure of cobalt glycolate was also clearly disclosed. Through annealing treatment, cobalt glycolate transformed into Co_3O_4 phase (Fig. S6a†). Fig. 2(d–f) illustrates that the IH-Co_3O_4 microspheres still retain the interconnected hierarchical structure but have shrunk only with simplex mesopores. The results

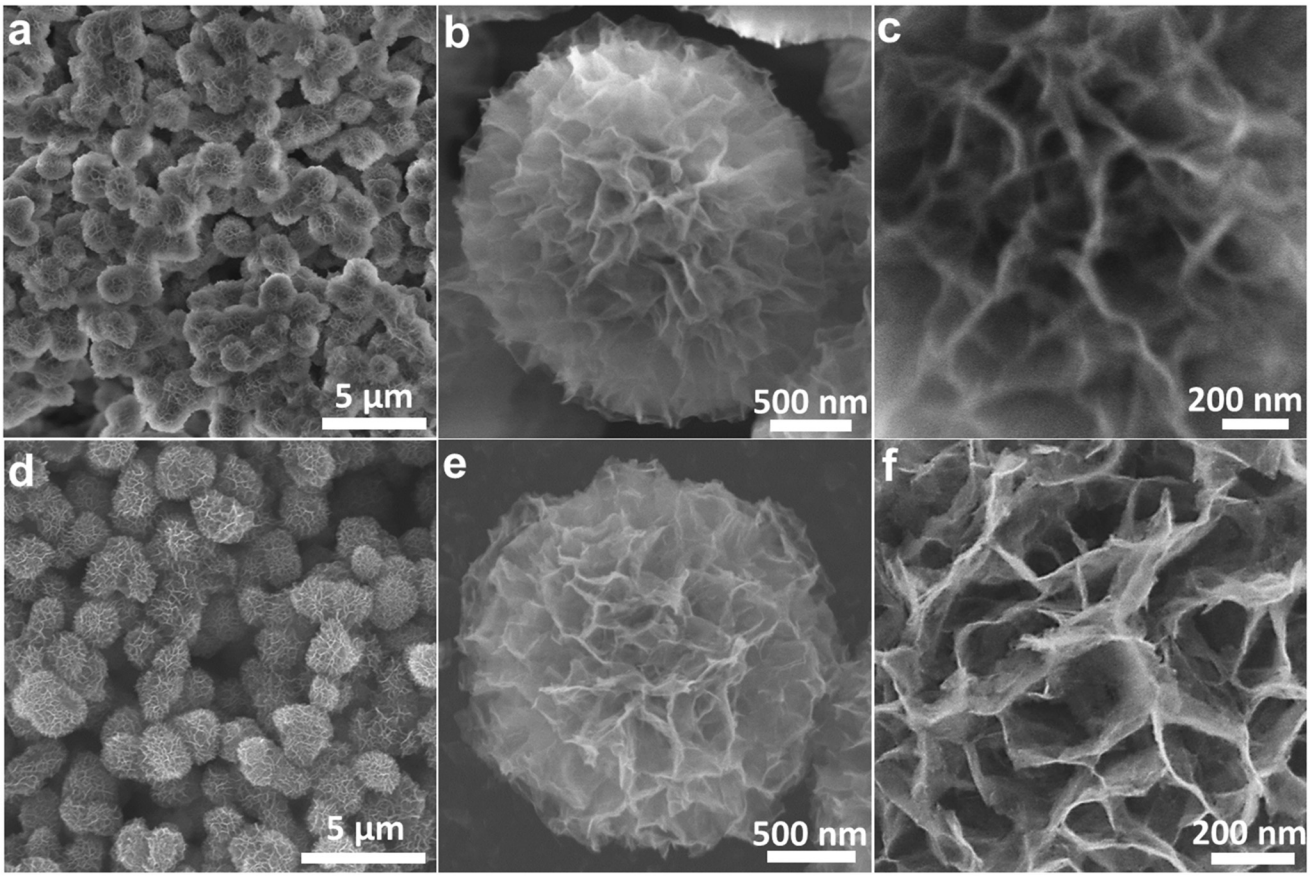

Fig. 1 Typical SEM images of (a–c) the nickel–cobalt glycolate precursor and (d–f) the IH-$NiCo_2O_4$ microspheres.

Open Access Article. Published on 21 June 2017. Downloaded on 9/23/2024 5:19:20 PM.
This article is licensed under a Creative Commons Attribution 3.0 Unported Licence.

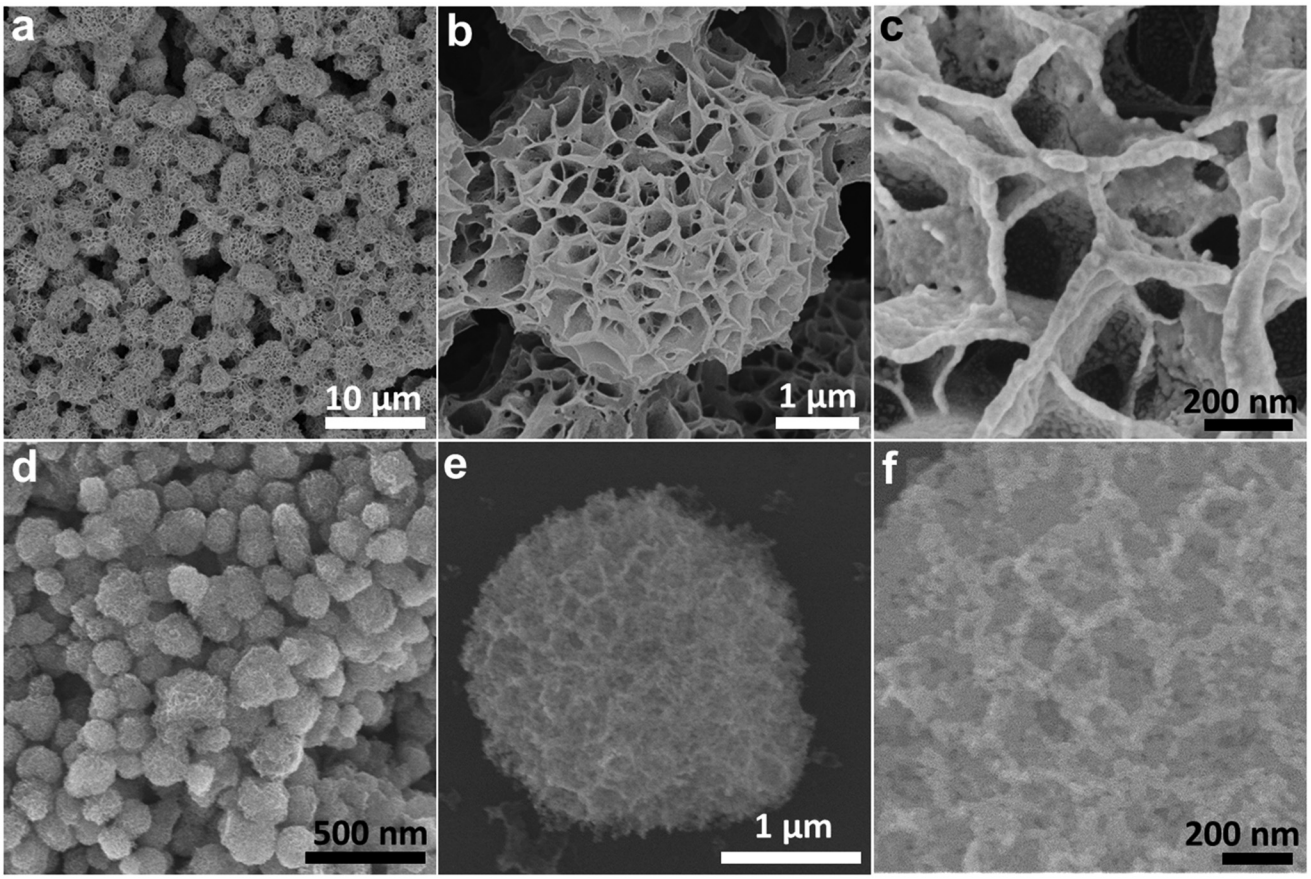

Fig. 2 Typical SEM images of (a–c) the cobalt glycolate precursor and (d–f) IH-Co_3O_4 microspheres.

indicate that the Co element partially substituted by nickel is beneficial for the complete preservation of the interconnected hierarchical structure.

To further explore the microstructure of the IH-$NiCo_2O_4$ sample, detailed TEM measurements were conducted. Fig. 3a and b shows the TEM images of a single $NiCo_2O_4$ sphere, demonstrating the self-supported hierarchical structure. Fig. 3c proves that the sample possesses an interconnected character and is composed of ultrathin nanosheets. Fig. 3d shows the TEM image of an individual ultrathin nanosheet exfoliated from the sphere. It can be seen that the nanosheet has an obvious nano/mesoporous structure with interconnected nanoparticles. The thickness of the nanosheet was calculated to be sub-5 nm, as shown in Fig. 3e. Note that the interconnected hierarchical structure of $NiCo_2O_4$ facilitates electrolyte diffusion and exposure of active sites. The inset in Fig. 3c is the corresponding selected area electron diffraction (SAED) pattern, which shows the polycrystalline nature of the IH-$NiCo_2O_4$ sample. The diffraction rings can be assigned to the (220), (311), (400), (511), and (440) planes of $NiCo_2O_4$. The HRTEM lattice image in Fig. 4f shows that the comprised nanoparticle has lattice fringes with an interplane spacing of 0.249 nm, corresponding to the (220) planes of $NiCo_2O_4$. To further demonstrate the structural features of the $NiCo_2O_4$ sample, the high angle annular dark field scanning TEM (HAADF-STEM) image and corresponding element mappings were obtained, as shown in Fig. 4g. The interconnected hierarchical structure with ultrathin nanosheets of $NiCo_2O_4$ is confirmed, and Co, Ni, and O elements are homogeneously distributed over the whole $NiCo_2O_4$. In addition, the TEM results of Co_3O_4 are also presented in Fig. S7.† It can be observed that the Co_3O_4 microsphere is self-supported by interconnected nanoparticles, and no ultrathin nanosheets are observed. This structure provides Co_3O_4 with abundant simplex mesopores with a size of less than 5 nm. The HRTEM image of the Co_3O_4 nanoparticle confirms its good crystallinity, consistent with the XRD results (Fig. S6a†).

The more detailed elemental composition and electron structure of the as-prepared IH-$NiCo_2O_4$ were further characterized by X-ray photoelectron spectroscopy (XPS) measurements. The elements Ni, Co, and O were clearly detected by XPS, as shown in Fig. 4. Furthermore, a Gaussian fitting method was employed to comprehensively analyze the oxidation state of the elements. As shown in Fig. 4a, Ni^{2+} and Ni^{3+} were completely characterized *via* the Ni 2p emission spectrum, exhibiting two shake-up satellites.[12,17,35] The fitting peaks at 855.1 eV and 872.8 eV correspond to Ni^{2+}, whereas the peaks at 856.1 eV and 874.1 eV are ascribed to Ni^{3+}.[11,12] In addition, two strong

 This journal is © The Royal Society of Chemistry 2017

Open Access Article. Published on 21 June 2017. Downloaded on 9/23/2024 5:19:20 PM.
This article is licensed under a Creative Commons Attribution 3.0 Unported Licence.

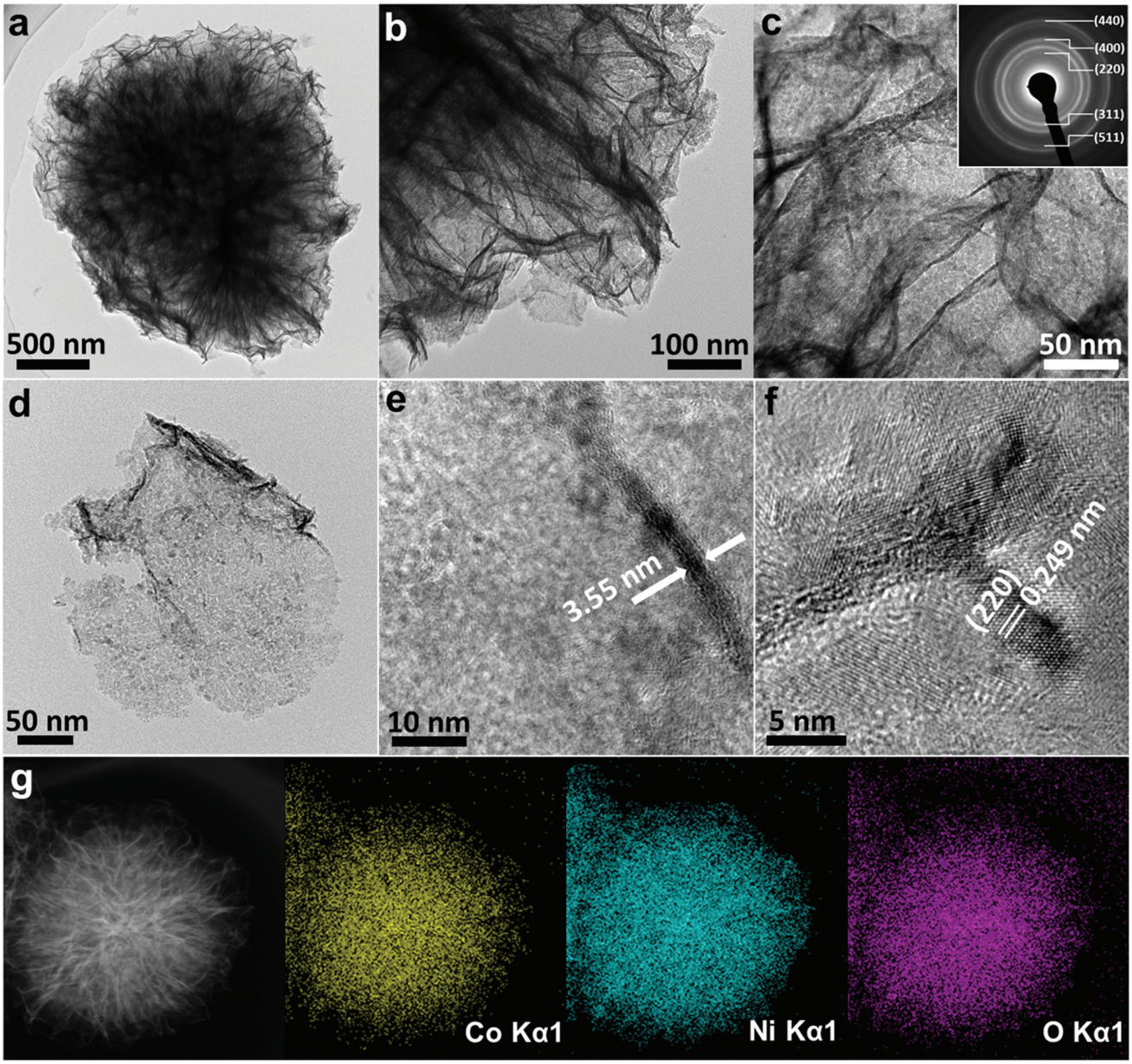

Fig. 3 (a) TEM image of an individual IH-$NiCo_2O_4$ microsphere. (b) and (c) TEM images of the local characteristic regions of the IH-$NiCo_2O_4$ microsphere. The inset in (c) is the corresponding SAED pattern. (d) TEM image of a single nanosheet exfoliated from an IH-$NiCo_2O_4$ sphere. (e) Lateral TEM image of a nanosheet used to evaluate its thickness. (f) HRTEM lattice image of the IH-$NiCo_2O_4$ microsphere. (g) HAADFSTEM image and the corresponding EDS elemental maps showing Co, Ni, and O.

shakeup-type peaks of nickel at 861.2 and 879.7 eV were also found.[32,35] Moreover, for the spectrum of Co 2p shown in Fig. 4b, two kinds of Co species can be found; the fitting peaks at 781.0 and 796.6 eV are assigned to Co^{2+}, and the peaks located at 779.6 and 795.2 are attributed to Co^{3+}.[30,36] The high-resolution spectrum of the O 1s region elucidates three oxygen contributions, which have been named O1, O2, and O3, as shown in Fig. 4c.[12,32,33] The fitting peak of O1 at 529.7 eV is attributed to a typical metal–oxygen bond.[19] The peak O2 at 531.3 eV is usually regarded as the low-oxygen-coordinated defect site and the surface-adsorbed oxygen species.[19] In addition, the peak O3 at 531.8 eV is commonly ascribed to the multiplicity of physic-/chemisorbed water at/within the interface of the material.[19,33] The abovementioned results show that the surface of the as-prepared IH-$NiCo_2O_4$ has a composition containing Ni^{2+}, Ni^{3+}, Co^{2+}, and Co^{3+}. Moreover, the XPS data of the obtained Co_3O_4 were also obtained and are shown in Fig. S6,† which confirm Co^{2+} and Co^{3+} in the surface of Co_3O_4.

Generally, the electrochemical performances of active materials are intimately associated with their mesoporous characteristics.[9,24,26] To confirm the mesoporous structure of the obtained microspheres, the specific surface area (SSA) and

Open Access Article. Published on 21 June 2017. Downloaded on 9/23/2024 5:19:20 PM.
This article is licensed under a Creative Commons Attribution 3.0 Unported Licence.

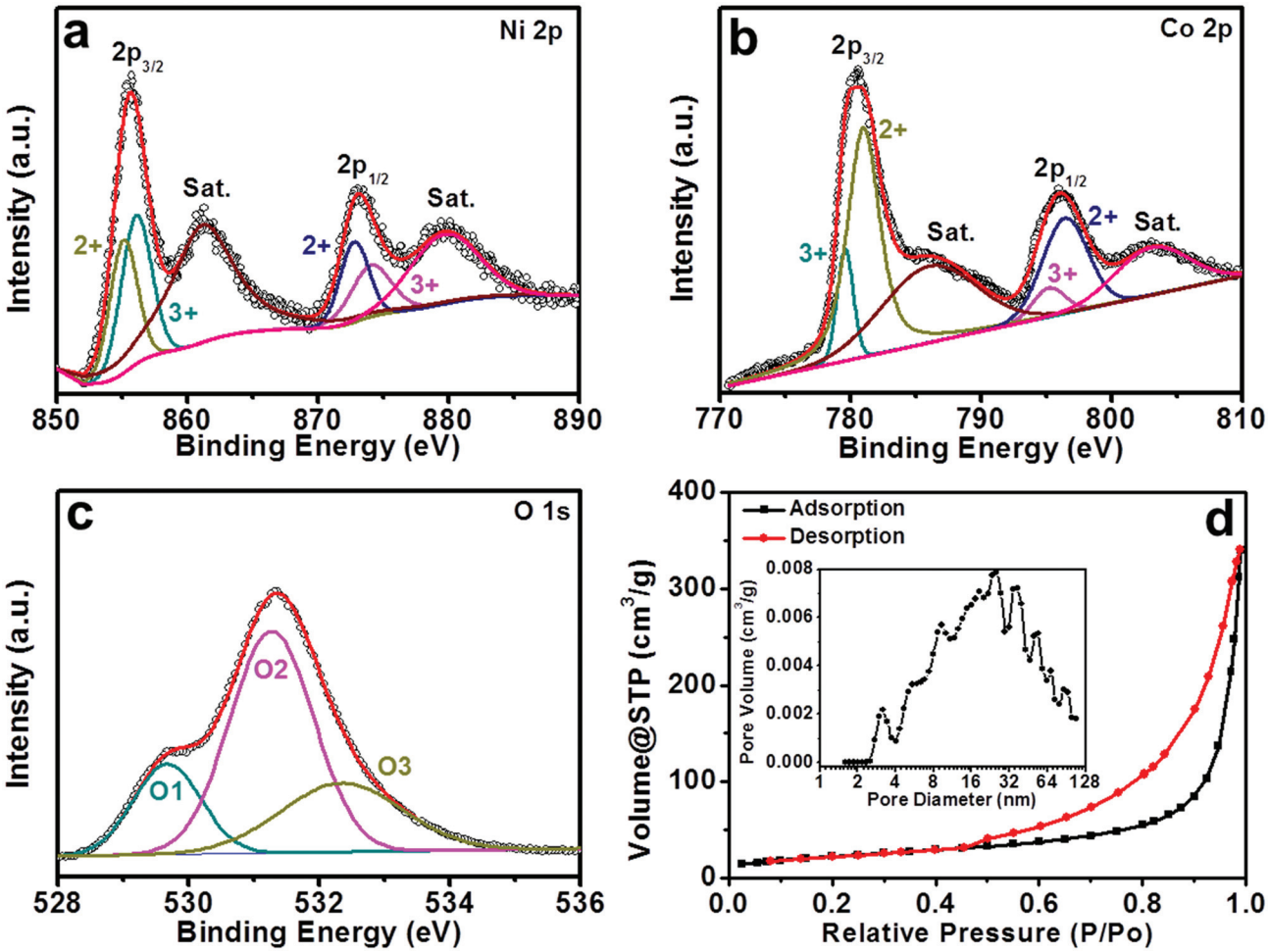

Fig. 4 High resolution XPS spectra for the Ni 2p (a), Co 2p (b), and O 1s (c) of the IH-$NiCo_2O_4$ sample. (d) Typical N_2 adsorption and desorption isotherms and the pore-size-distribution curves (inset) of IH-$NiCo_2O_4$.

pore size distribution analysis were performed by nitrogen adsorption and desorption experiments. Fig. 4d displays the N_2 adsorption–desorption isotherm of the as-prepared IH-$NiCo_2O_4$. The loop, which is well consistent with the type IV curve, demonstrates the existence of mesopores in the sample.[19] The linear increase in N_2 uptake in the medium P/P_0 region indicates capillary condensation and multilayer adsorption in the mesopores.[25] The representative hysteresis loop in the high P/P_0 region reveals that the IH-$NiCo_2O_4$ microspheres mainly consist of mesopores.[16] The SSA of the IH-$NiCo_2O_4$ microspheres is calculated to be 81.27 $m^2\ g^{-1}$ by the Brunauer–Emmett–Teller (BET) method. The Barrett–Joyner–Halenda (BJH) pore size distribution plot shown in the inset of Fig. 4d reveals that abundant mesopores exist in IH-$NiCo_2O_4$, which is consistent with its hierarchical structure. The large SAA and abundant mesopores can facilitate substantial contact between the electrolyte and the active sites. Furthermore, the SSA of IH-Co_3O_4 is also calculated to be 273.51 $m^2\ g^{-1}$ with a narrow pore diameter distribution around 3.8 nm, as shown in Fig. S6d,† corresponding to the TEM results (Fig. S7†).

The electrochemical performance of the as-prepared samples employed as positive electrodes for supercapacitors was evaluated in a 6 M KOH aqueous solution. Fig. 5a presents the CV curves of the IH-$NiCo_2O_4$ electrode at different scan rates ranging from 5 to 50 mV s^{-1}. Distinct redox peaks can be observed, which demonstrate the pseudocapacitive performance of the IH-$NiCo_2O_4$ sample. These pairs of redox peaks are associated with the surface reversible redox reactions of Ni^{2+}/Ni^{3+} and Co^{3+}/Co^{4+}.[32,35] In addition, with the increasing scan rate, the anodic/cathodic peak continually shifts in the positive/negative direction.[37] Fig. 5b shows the CV plots of the IH-Co_3O_4 electrode, which exhibits the pseudocapacity based on the redox reactions of Co^{2+}/Co^{3+} and Co^{3+}/Co^{4+}.[2,27] Moreover, the integral area of IH-$NiCo_2O_4$ is higher than that of IH-Co_3O_4, indicating higher specific capacitance. To further evaluate the specific capacitance of the two samples, galvanostatic charge and discharge tests were carried out at various current densities, and the typical discharge curves are shown in Fig. 5c and d. Based on the galvanostatic discharge curves at the current densities of 2, 4, 6, 8, 10, 15, and 20 A g^{-1}, the specific capacitances of IH-$NiCo_2O_4$ were calculated to be

 This journal is © The Royal Society of Chemistry 2017

Open Access Article. Published on 21 June 2017. Downloaded on 9/23/2024 5:19:20 PM.
This article is licensed under a Creative Commons Attribution 3.0 Unported Licence.

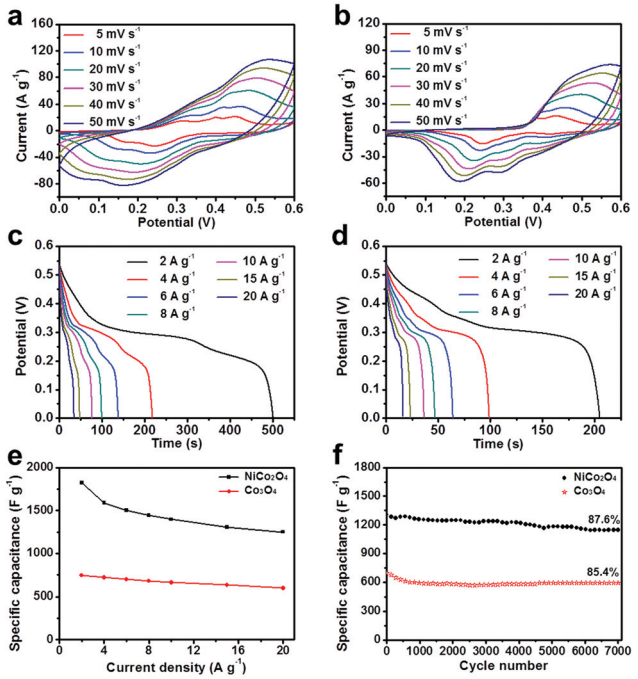

Fig. 5 CV curves at different sweep rates for IH-$NiCo_2O_4$ (a) and IH-Co_3O_4 (b). Discharge curves at different current densities for IH-$NiCo_2O_4$ (c) and IH-Co_3O_4 (d). (e) Specific capacitance at different current densities of the two samples. (f) Cycling stability of the two samples at a current density of 10 A g^{-1}.

1822.3, 1588.0, 1504.0, 1446.3, 1397.1, 1303.5, and 1250.9 F g^{-1}, respectively, whereas the specific capacitances of only IH-Co_3O_4 were 754.3, 719.8, 699.0, 679.8, 662.2, 633.3, and 596.4 F g^{-1} at the corresponding current densities, as shown in Fig. 5e. This high specific capacitance of IH-$NiCo_2O_4$ is also superior to those of the previously reported high-performance Ni–Co oxide materials such as yolk-shelled $Ni_{0.37}Co$ oxide nanoprisms (1563 F g^{-1} at 2 A g^{-1}),[15] $NiCo_2O_4$ microtubes (1387.9 F g^{-1} at 2 A g^{-1}),[30] UNF@$NiCo_2O_4$ composites (1460 F g^{-1} at 2 A g^{-1}),[22] and porous $NiCo_2O_4$ nanowires (1481 F g^{-1} at 0.5 A g^{-1}).[19] A comparison with previously reported $NiCo_2O_4$ nanomaterials is also given in Table S1,† which further confirms the excellent performance of the as-prepared IH-$NiCo_2O_4$.

To identify the electrical conductivity of the two samples, electrochemical impedance spectra (EIS) were obtained over a frequency range from 100 kHz to 0.01 Hz under open-circuit conditions. Typical Nyquist plots of the two samples are presented in Fig. S8.† It can be seen that all the EIS curves show a partial semicircle in the high-frequency region and an inclined line in the low-frequency region with the transition between two regions. The EIS data can be fitted by an equivalent circuit model (Fig. S8†), including a bulk system resistance R_s, a charge-transfer resistance R_{ct}, a pseudo-capacitance element C_{ps} from the redox process, and a C_{dl} representing the double-layer capacitance.[38–40] The R_s values of IH-$NiCo_2O_4$ and IH-Co_3O_4 are both measured to be 0.40 Ω, indicating that the two electrodes possess nearly equal solution resistance. It is widely known that the charge-transfer resistance R_{ct} controls the electron transfer kinetics of the redox reaction at the electrode interface and is a decisive parameter for supercapacitors.[26] The R_{ct} of the IH-$NiCo_2O_4$ electrode is measured to be 0.54 Ω, lower than that of the IH-Co_3O_4 electrode (4.56 Ω). The lower charge-transfer resistance of the IH-$NiCo_2O_4$ electrode benefits faster ion/electron transfer. Moreover, the straight sloping line in the low-frequency region shows the Warburg impedance that represents diffusive resistances of the electrolyte into the interior of the electrode pores and OH^- into the host materials or active sites. The IH-$NiCo_2O_4$ electrode has a more vertical line in the low-frequency range, suggesting better capacitive behavior and lower electrolyte diffusion impedance.[41,42] These results demonstrate the excellent supercapacitive performance of the IH-$NiCo_2O_4$ sample.

It is widely accepted that the long-term cycling life at high current density is an important parameter to evaluate the electrochemical performance of supercapacitors in practical application. To evaluate the cycling stability, consecutive charging/discharging measurements at a constant current density of 10 A g^{-1} were performed, as shown in Fig. 5f. Impressively, cycling is very stable for the IH-$NiCo_2O_4$ electrode with an 87.6% of the initial specific capacitance retention after 7000 cycles. In addition, the IH-Co_3O_4 electrode also exhibited an 85.4% of the initial specific capacitance after 7000 cycles. The enhanced cycling stability of the IH-$NiCo_2O_4$ is probably attributed to the unique interconnected hierarchal mesoporous structure, which is expected to improve the structural integrity. Degradation of IH-$NiCo_2O_4$ occurred due to the fact that during the continuous cycles at high current density, repeated intercalation and deintercalation of OH^- ions at the interface of electrode/electrolyte led to structural collapse to some extent, as shown in Fig. S9.†

To further evaluate the practical application of the IH-$NiCo_2O_4$ microspheres in energy storage field, an asymmetric supercapacitor (ASC) was fabricated using IH-$NiCo_2O_4$ and graphene as the cathode and the anode, respectively. The electrochemical performance of the graphene electrode was also tested in a 6 M KOH aqueous solution (Fig. S10†). The CV curves of the graphene electrode exhibit typical rectangular shapes, indicating an electrical double-layer capacitance behavior. Based on the discharge curve obtained at 1 A g^{-1}, the specific capacitance of the graphene electrode is calculated to be 197.8 F g^{-1}. To balance the charge between the positive and negative electrodes, the mass ratio of the positive electrode to the negative electrode is optimized to be 0.22 based on the CV studies of the IH-$NiCo_2O_4$ and the graphene electrodes at a scan rate of 10 mV s^{-1} (Fig. S10d†). A series of CV measurements of the asymmetric supercapacitor with different voltage windows at 10 mV s^{-1} was performed to estimate the best operating potential of the ASC (Fig. 6a). As expected, the asymmetric supercapacitor has a stable potential window up to 1.6 V without obvious polarization curves. Therefore, an operation potential window of 1.6 V was appropriately chosen to investigate the electrochemical performance of the ASC.

Open Access Article. Published on 21 June 2017. Downloaded on 9/23/2024 5:19:20 PM.
This article is licensed under a Creative Commons Attribution 3.0 Unported Licence.

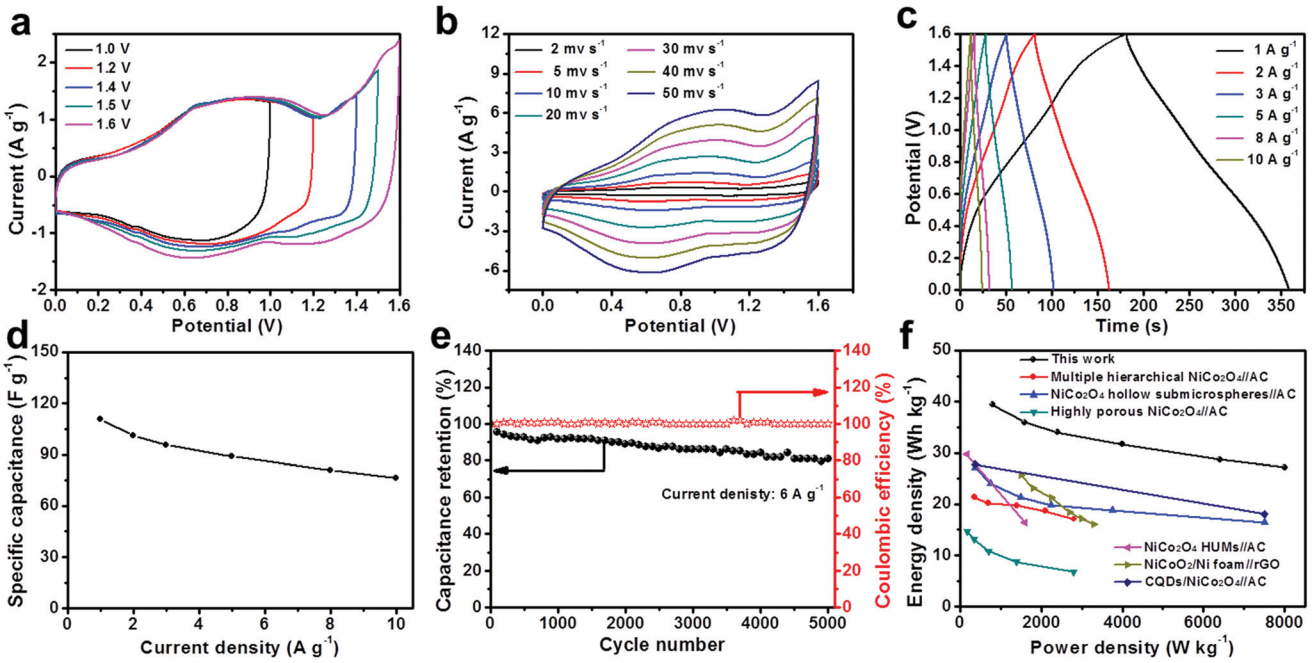

Fig. 6 (a) CV curves of the IH-$NiCo_2O_4$//graphene ASC measured at different potential windows at a scan rate of 10 mV s^{-1}. (b) CV curves of the IH-$NiCo_2O_4$//graphene ASC at different scan rates in the potential window of 0–1.6 V. (c) Galvanostatic charge/discharge curves of the IH-$NiCo_2O_4$//graphene ASC at different current densities. (d) Specific capacitance of the IH-$NiCo_2O_4$//graphene ASC at different current densities. (e) Cycling stability and coulombic efficiency of the IH-$NiCo_2O_4$//graphene ASC at a constant current density of 6 A g^{-1}. (f) Ragone plots of the IH-$NiCo_2O_4$//graphene ASC and other previously reported Ni–Co oxide ASCs.

Fig. 6b shows the CV curves of the ASC at different scan rates ranging from 2 to 50 mV s^{-1} within the potential window of 0–1.6 V in a 6 M KOH aqueous electrolyte. The capacitance contribution from both the electric double-layer capacitance and pseudocapacitance can be clearly observed from the distorted rectangular CV curves at each scan rate. Fig. 6c shows the typical galvanostatic charge/discharge curves of the asymmetric supercapacitor measured at different current densities in a potential window of 0–1.6 V. The specific capacitances of the asymmetric supercapacitor calculated from galvanostatic discharge curves are 110.8, 101.2, 95.7, 89.1 80.8, and 76.5 F g^{-1} at the current densities of 1, 2, 3, 5, 8, and 10 A g^{-1} (Fig. 6d). Note that the ASC exhibits good rate capability with 69% of the capacitance retained at a high current density of 10 A g^{-1}. Moreover, a long cycling-life test was carried out for the IH-$NiCo_2O_4$//graphene ASC by repeated charging/discharging measurements at a constant current density of 6 A g^{-1} between 0 and 1.6 V (Fig. 6e). It can be seen that the coulombic efficiency of the IH-$NiCo_2O_4$//graphene ASC approaches and then maintains a value of 100%, and as much as 80% of the initial specific capacitance retention is presented after 5000 cycles. These results suggest that the IH-$NiCo_2O_4$//graphene ASC possesses excellent electrochemical stability.

Moreover, to evaluate the energy storage ability of the IH-$NiCo_2O_4$//graphene ASC, the Ragone plots based on the galvanostatic discharge curves are displayed in Fig. 6f. The assembled ASC delivers a high energy density of 39.4 Wh kg^{-1} at a power density of 800 W kg^{-1} and still holds 27.2 Wh kg^{-1} at a higher power density of 8000 W kg^{-1}. This high-performance ASC is superior to many previously reported systems (Fig. 6f) such as multiple hierarchical $NiCo_2O_4$//AC,[16] $NiCo_2O_4$ hollow submicrospheres//AC,[43] highly porous $NiCo_2O_4$//AC,[17] $NiCo_2O_4$ HUMs//AC,[32] $NiCoO_2$/Ni foam//rGO,[37] and CQDs/$NiCo_2O_4$//AC.[34] The abovementioned results suggest that IH-$NiCo_2O_4$ is a promising alternative electrode material for supercapacitor applications.

Conclusions

In summary, we reported the fabrication of IH-$NiCo_2O_4$ microspheres *via* a typical solvothermal process followed by an annealing treatment. When only Co-based salt was introduced into a similar system, the corresponding IH-Co_3O_4 was obtained. TEM techniques and N_2 adsorption and desorption experiments reveal their mesoporous structure with abundant mesopores. Due to the unique structure of large tunnels and mesopores and the synergetic effect of two different metal cations in a single crystal structure, when IH-$NiCo_2O_4$ is employed as an electrode material for supercapacitors, it shows a high specific capacitance of 1822.3 F g^{-1} at a current density of 2 A g^{-1} and a capacitance retention of 87.6% at 10 A g^{-1} after 7000 cycles, which outperforms IH-Co_3O_4. Moreover, an IH-$NiCo_2O_4$//graphene ASC was further fabricated and showed high specific capacitance, good cycling performance, and excellent reversibility of the Faradaic reaction. These

 This journal is © The Royal Society of Chemistry 2017

results suggest that IH-$NiCo_2O_4$ prepared through a facile synthesis strategy can be a promising alternative material for energy storage devices.

Acknowledgements

This work was supported by the National Natural Science Foundation of China (no. 51371015, 51331002, 11674023, 51571006, 21601013) and Beijing Municipal Science and Technology Project (No. Z17111000220000).

Open Access Article. Published on 21 June 2017. Downloaded on 9/23/2024 5:19:20 PM.
This article is licensed under a Creative Commons Attribution 3.0 Unported Licence.

Notes and references

1 G. Zhang and X. W. Lou, *Adv. Mater.*, 2013, **25**, 976.
2 X. Zhou, X. Shen, Z. Xia, Z. Zhang, J. Li, Y. Ma and Y. Qu, *ACS Appl. Mater. Interfaces*, 2015, **7**, 20322.
3 G. Q. Zhang, H. B. Wu, H. E. Hoster, M. B. Chan-Park and X. W. Lou, *Energy Environ. Sci.*, 2012, **5**, 9453.
4 G. Gao, H. B. Wu, S. Ding, L. M. Liu and X. W. Lou, *Small*, 2015, **11**, 804–808.
5 B. D. Boruah and A. Misra, *J. Mater. Chem. A*, 2016, **4**, 17552.
6 P. Simon and Y. Gogotsi, *Nat. Mater.*, 2008, **7**, 845.
7 Q. Liao, N. Li, S. Jin, G. Yang and C. Wang, *ACS Nano*, 2015, **9**, 5310.
8 N. Yu, H. Yin, W. Zhang, Y. Liu, Z. Tang and M. Q. Zhu, *Adv. Energy Mater.*, 2015, **6**, 1501.
9 X. Chen, M. Cheng, D. Chen and R. Wang, *ACS Appl. Mater. Interfaces*, 2016, **8**, 3892.
10 Y. Xu, X. Gao, W. Chu, Q. Li, T. Li, C. Liang and Z. Lin, *J. Mater. Chem. A*, 2016, **4**, 10248.
11 L. Ye, L. Zhao, H. Zhang, P. Zan, G. Shuai, W. Shi, B. Han, H. Sun, X. Yang and T. Xu, *J. Mater. Chem. A*, 2016, **5**, 1603.
12 L. Liu, H. Zhang, L. Fang, Y. Mu and Y. Wang, *J. Power Sources*, 2016, **327**, 135.
13 W. Zeng, L. Wang, H. Shi, G. Zhang, K. Zhang, H. Zhang, F. Gong, T. Wang and H. Duan, *J. Mater. Chem. A*, 2016, **4**, 8233.
14 X. Xiong, B. Zhao, D. Ding, D. Chen, C. Yang, Y. Lei and M. Liu, *NPG Asia Mater.*, 2016, **8**, e300.
15 L. Yu, B. Guan, W. Xiao and X. W. D. Lou, *Adv. Energy Mater.*, 2015, **5**, 1500981.
16 S. Wang, S. Sun, S. Li, F. Gong, Y. Li, Q. Wu, P. Song, S. Fang and P. Wang, *Dalton Trans.*, 2016, **45**, 7469.
17 R. Ding, L. Qi, M. Jia and H. Wang, *Electrochim. Acta*, 2013, **107**, 494.
18 C. Zheng, C. Cao, R. Chang, J. Hou and H. Zhai, *Phys. Chem. Chem. Phys.*, 2016, **18**, 6268.
19 C. An, Y. Wang, Y. Huang, Y. Xu, L. Jiao and H. Yuan, *Nano Energy*, 2014, **10**, 125.
20 Y. Guo, L. Yu, C.-Y. Wang, Z. Lin and X. W. D. Lou, *Adv. Funct. Mater.*, 2015, **25**, 5184.
21 C. Yuan, J. Li, L. Hou, X. Zhang, L. Shen and X. W. D. Lou, *Adv. Funct. Mater.*, 2012, **22**, 4592.
22 J. Pu, Z. Liu, Z. Ma, J. Wang, L. Zhang, S. Chang, W. Wu, Z. Shen and H. Zhang, *J. Mater. Chem. A*, 2016, **4**, 17394.
23 H. Hu, B. Guan, B. Xia and X. W. Lou, *J. Am. Chem. Soc.*, 2015, **137**, 5590.
24 Y. Zhang, M. Ma, J. Yang, C. Sun, H. Su, W. Huang and X. Dong, *Nanoscale*, 2014, **6**, 9824–9830.
25 Z. Chen, Z. Wan, T. Yang, M. Zhao, X. Lv, H. Wang, X. Ren and X. Mei, *Sci. Rep.*, 2016, **6**, 25151.
26 M. Cheng, S. Duan, H. Fan and R. Wang, *CrystEngComm*, 2016, **18**, 6849.
27 X. Zhang, Y. Zhao and C. Xu, *Nanoscale*, 2014, **6**, 3638.
28 D. P. Dubal, P. Gomez-Romero, B. R. Sankapal and R. Holze, *Nano Energy*, 2015, **11**, 377.
29 Z. Wu, Y. Zhu and X. Ji, *J. Mater. Chem. A*, 2014, **2**, 14759.
30 F.-X. Ma, L. Yu, C.-Y. Xu and X. W. Lou, *Energy Environ. Sci.*, 2016, **9**, 862.
31 L. Shen, L. Yu, X. Y. Yu, X. Zhang and X. W. Lou, *Angew. Chem., Int. Ed.*, 2015, **54**, 1868.
32 Y. Lei, Y. Wang, W. Yang, H. Yuan and D. Xiao, *RSC Adv.*, 2015, **5**, 7575.
33 L. Liu, J. Wang, Y. Hou, J. Chen, H. K. Liu, J. Wang and Y. Wu, *Small*, 2016, **12**, 602.
34 Y. Zhu, Z. Wu, M. Jing, H. Hou, Y. Yang, Y. Zhang, X. Yang, W. Song, X. Jia and X. Ji, *J. Mater. Chem. A*, 2015, **3**, 866.
35 M. J. Pang, S. Jiang, G. H. Long, Y. Ji, W. Han, B. Wang, X. L. Liu, Y. L. Xi, F. Z. Xu and G. D. Wei, *RSC Adv.*, 2016, **6**, 67839.
36 S. H. Yue, H. Tong, L. Lu, W. W. Tang, W. L. Bai, F. Q. Jin, Q. W. Han, J. P. He, J. Liu and X. G. Zhang, *J. Mater. Chem. A*, 2017, **5**, 689.
37 X. Xu, H. Zhao, J. Zhou, R. Xue and J. Gao, *J. Power Sources*, 2016, **329**, 238.
38 S. Duan and R. Wang, *NPG Asia Mater.*, 2014, **6**, e122.
39 H. Pang, C. Z. Wei, X. X. Li, G. C. Li, Y. H. Ma, S. J. Li, J. Chen and J. S. Zhang, *Sci. Rep.*, 2014, **4**, 8.
40 W. Du, Z. Wang, Z. Zhu, S. Hu, X. Zhu, Y. Shi, H. Pang and X. Qian, *J. Mater. Chem. A*, 2014, **2**, 9613.
41 H. Pang, Y. Liu, J. Li, Y. Ma, G. Li, Y. Ai, J. Chen, J. Zhang and H. Zheng, *Nanoscale*, 2013, **5**, 503.
42 H. Pang, Z. Yan, W. Wang, J. Chen, J. Zhang and H. Zheng, *Nanoscale*, 2012, **4**, 5946.
43 Y. Zhu, J. Wang, Z. Wu, M. Jing, H. Hou, X. Jia and X. Ji, *J. Power Sources*, 2015, **287**, 307.